FLOW PREDICTION IN REAL STRUCTURES USING OPTICAL COHERENCE TOMOGRAPHY AND LATTICE BOLTZMANN MATHEMATICS

Joy P. Dunkers[1], Frederick R. Phelan[1], Carl G. Zimba[1], Kathleen M. Flynn[1], Richard C. Peterson[1], Xingde Li[2], James G. Fujimoto[2] and Richard S. Parnas[1]

[1] Polymers Division, National Institute of Standards & Technology, Stop 8543, Gaithersburg, MD 20899 USA
[2] Department of Electrical Engineering, Massachusetts Institute of Technology, Cambridge, MA 02139

ABSTRACT

The permeability tensor is a critical design parameter for liquid composite molding. Efforts over the past several years have demonstrated the difficulties in permeability measurement and multi-phase flow behavior. Microflow simulations based on lattice-Boltzmann methods have shown that the permeability and the unsaturated flow behavior can be estimated if the porous structure of the material can be characterized, but existing characterization methods are either too slow and difficult, have insufficient resolution, or are extremely expensive with limited availability. Optical coherence tomography can in many cases provide images with a spatial resolution of 15 microns, acquired nondestructively in less than one minute, for a cost near $60,000. The important issues of sample refractive index and image processing will be discussed to illustrate the limitations of this imaging technique. Predictions of permeability, images of damage accumulation, and the distributions of short fibers in a thermoplastic matrix will illustrate the potential of the technique.

INTRODUCTION

The need for data to design composite parts and processes has been repeatedly stressed in recent years [1-3]. However, the lack of reliable data characterizing the fiber reinforcements commonly used in composites manufacturing hinders wider use of composites. Two particular properties required for process design are the reinforcement permeability and compressibility [4-6]. Although permeability has received considerable attention in the literature, the importance of compressibility has only been recently recognized. The permeability tensor and fluid viscosity control the relationship between the fluid velocity and pressure gradient through Darcy's law [7], and such flow through the fiber preform is particularly important in manufacturing processes such as liquid composite molding (LCM) and pultrusion. The preform compressibility is also required for design because the compressibility determines the relative fiber volume fractions of the materials within a preform. Since the permeability is strongly dependent on the volume fraction, knowledge of the reinforcement compressibility enables the designer to place multiple types

of reinforcement into a preform and compute the effects of those materials on both the mechanical properties and processibility of the composite.

A major component of mold design for LCM is the placement of fill ports and exhaust vents, which is determined by simulating the mold filling operation. Simulations inform the designer of the best fill port locations to minimize filling times and injection pressures, as well as the mold locations that are the last to fill, and which therefore require venting. Mold filling simulations solve Darcy's law

$$\mathbf{v} = \frac{\mathbf{K}}{\mu} \cdot \nabla p \qquad (1)$$

where $\mathbf{v}$ is the fluid velocity, ∇p is the pressure gradient, μ is the fluid viscosity, and $\mathbf{K}$ permeability tensor. In most cases, the simulations combine Darcy's law with the continuity equation, $\nabla \cdot \mathbf{v} = 0$, yielding a partial differential equation (PDE) in the mold pressure distribution. The parameters of the PDE are the components of the permeability tensor, which illustrates the necessity of accurate permeability values to achieve reliable design. Furthermore, because the solution of the PDE predicts the pressure distribution in the mold, these mold filling simulations also provide input to the mechanical design of the mold structure, which must possess sufficient strength to resist deflection under the hydrodynamic loads developed during the mold filling operation [2].

The classical definition of permeability, based on Darcy [7], and for which Darcy's law has been theoretically derived [8], is for fully saturated flow in semi-infinite porous media. However, the LCM process involves unsaturated flow in parts that are often quite thin. Therefore, one expects flow behavior not fully described in Darcy's law. Nevertheless, current flow simulations available to the designer rely exclusively on Darcy's law, as described above. Therefore, practical measures of apparent permeability for unsaturated flow have been developed [9] to complement classical measurement techniques used with saturated flow.

The saturated flow measurement is typically conducted in a mold in which the sample reinforcement has been carefully saturated with fluid. After carefully saturating the media, steady state flow and pressure drop measurements are obtained. The scalar permeability for flow in a specific direction through the preform is then easily obtained from the slope of the line fitting the data using Eq(1), and with knowledge of the mold cross sectional area and the fluid viscosity. By combining measurements taken in several flow directions, we obtain the complete permeability tensor according to Parnas and Salem [11] or, more generally, Woerdeman *et al.* [12]. A much more thorough description of the measurement apparatus, techniques and associated errors is available elsewhere [5,10,11].

Unsaturated flow measurements are typically conducted in center gated molds. As the flow expands radially, transient flow front data can be imaged, and transient mold inlet pressure or flow can also be recorded. Analysis based on Adams et al. [9] then yields the in-plane permeability tensor for unsaturated flow, assuming one principal direction of the permeability is through the thickness of the material. More sophisticated analyses have been developed recently for unsaturated unidirectional flow experiments in which the permeability

and capillary effects are analyzed simultaneously [13].

Although the permeability measurement experiments are conceptually simple, three types of errors are commonly encountered by researchers attempting to measure permeability. First, and most widely discussed, is the edge effect, where an imperfect fit of the sample at the mold edges allows fluid to leak past the preform during unidirectional flow experiments. This problem is easily detected during the initial filling of the mold if a transparent mold side (top or bottom) is employed to allow visual inspection of the flow. If undetected, edge effects can cause errors in the measured permeability in excess of 100%. Second, an unsaturation error arises during "saturated" flow experiments if the initial mold filling leaves significant amounts of trapped air in the sample. Often such trapped air cannot escape and expands and contracts during the course of the experiment, leading to apparent non-Darcy behavior and measurement errors as large as 50%. Third, mold deflection errors occur as a result of using transparent mold sides that are insufficiently stiff to resist the internal mold pressure developed during the experiment. Mold deflection can lead to apparent non-Darcy behavior, especially noticeable in thin molds, and can also lead to errors of 50% in the measured permeability. A database of experimental measurements is available for a variety of reinforcements [14].

In light of these limitations, computational prediction of permeability [15-18] offers a potentially accurate and robust alternative to experimental methods. Such calculations involve imposing a pressure drop across the media, solving the appropriate transport equations for the detailed flow field, and then back-calculating the permeability by applying Darcy's law. The biggest drawback of this approach has been the inability to accurately determine the detailed geometry of the fibrous preform materials, which in addition to many intricate structural features, typically contain statistical variations and defects in their microstructure [19]. Without a precise representation of the media, it is not possible to accurately predict permeability values using computational methods.

There have been two main approaches to the problem of microstructure determination. The first is to perform calculations on small, computationally efficient "unit cell" structures using nominal dimensions that represent the average preform weave structure. The major problem with this approach is that calculations on the "average" unit cell structure do not in general, yield an accurate value for the average permeability [19]. A second approach is to determine the microstructure via optical methods (e.g., microscopy), and directly perform the numerical calculation on a discretization of the optical image. This approach has the advantage of exactly representing the media, and by including large sections of the media in the image, variations and defects in the microstructure are automatically accounted for in the calculation. However, until recently, this approach was probably even more tedious to perform than direct experimental measurement of permeability since the composite specimens typically had to be carefully sectioned, polished and examined. However, a new technique being investigated in this work called optical coherence tomography (OCT) offers a means for rapidly and non-destructively determining the microstructure of fiber reinforced plastic materials, potentially leading to a robust means of computational permeability prediction.

Optical coherence tomography is a non-invasive, non-contact optical imaging technique that allows the visualization of microstructure within scattering media [20-22], OCT uses light in a manner analogous to the way ultrasound imaging uses sound, providing significantly higher spatial resolution (~ 15 μm) albeit with shallower penetration depth. OCT is based upon low-coherence optical ranging techniques where the optical distance to individual sites within the sample is determined by the difference in time, relative to a reference light beam, for an incident light beam to penetrate and backscatter within the sample. This temporal delay is probed using a fiber optic interferometer and a broadband laser light source.

In this work, OCT was used to image an epoxy/unidirectional E-glass composite. The volumetric images were converted to binary and input into a flow code for prediction of axial and transverse permeabilities. The predicted permeabilities of different image processing routines are compared with experimental values.

EXPERIMENTAL DETAILS

Measurements of Permeability

The permeability of a weft unidirectional glass fabric was measured for comparison with predictions. The material used was Owens Corning Knytex D-155, and contained ECM-450, 1/0 tows, constrained by polyester crossing threads. Several measurements were conducted in a narrow range of fiber volume fractions to obtain a reliable average value as well as error estimates. Measurements were conducted with saturated, unidirectional flow along the fiber tows as well as with unsaturated radial flow. Table 1 summarizes the measurements. The average saturated permeability for flow along the fiber tows is $5.3 \cdot 10^{-6}$ cm^2 with an uncertainty of $2.6 \cdot 10^{-6}$ cm^2. From the radial flow experiment, the ratio of the

Table 1. Experimental Measurements of Permeability

Fiber Volume (%)	Type of Measurement	K (cm^2)	Angle (degrees)	Ratio of Ellipse axes
43.8	Unidirectional, Axial, saturated	1.64E-06	N/A	N/A
44.2	Unidirectional, Axial, saturated	7.86E-06	N/A	N/A
44.4	Unidirectional, Axial, saturated	5.37E-06	N/A	N/A
43.8	Unidirectional, Axial, saturated	6.20E-06	N/A	N/A
44.2	Radial unsaturated	N/A	0	.378

permeability for flow perpendicular to the tows to the permeability for flow along the tows is simply the square of the ellipticity observed in the unsaturated flow front, i.e. $(0.378)^2 = 0.143$. As expected, the radial flow experiment also indicated that the major axis of the in-plane permeability tensor lies along the tow direction.

Materials for Composite Preparation

The epoxy resin system consisted of a diglycidyl ether of bisphenol A (DGEBA) monomer (Tactix123 , Dow Chemical Company, Midland, MI) and two amines [23]. Aromatic methylene dianiline (MDA) and aliphatic poly(propylene glycol)bis(2-aminopropyl ether) (JeffamineD400) (Mn»400) were purchased and used as received from Aldrich (Minneapolis, MN). The oxirane/ amine stoichiometry was 2 mol oxirane/1 mol amine. The amine composition consisted of 0.07 mol MDA and 0.93 mol D400. The refractive index of the postcured resin and of the fibers is 1.552 ± 0.004 and 1.554 ± 0.004, respectively, as measured by white light and index matching fluids. The refractive index of the epoxy composite is calculated by the rule of mixtures. The resin volume fraction was 0.56 and the fiber volume fraction was 0.44; thus, the refractive index of the composite is 1.55. The index mismatch between resin and fiber influences the depth of field. Details of the mixing and RTM are provided elsewhere [24].

Instrumentation for Optical Coherence Tomography

The imaging system used in this study is schematically shown in Figure 1. A commercial superluminescent light source (AFC Technologies inc., Hull, Quebec, Canada) was used for the studies reported here. The source operated at 1.3 μm with an output power

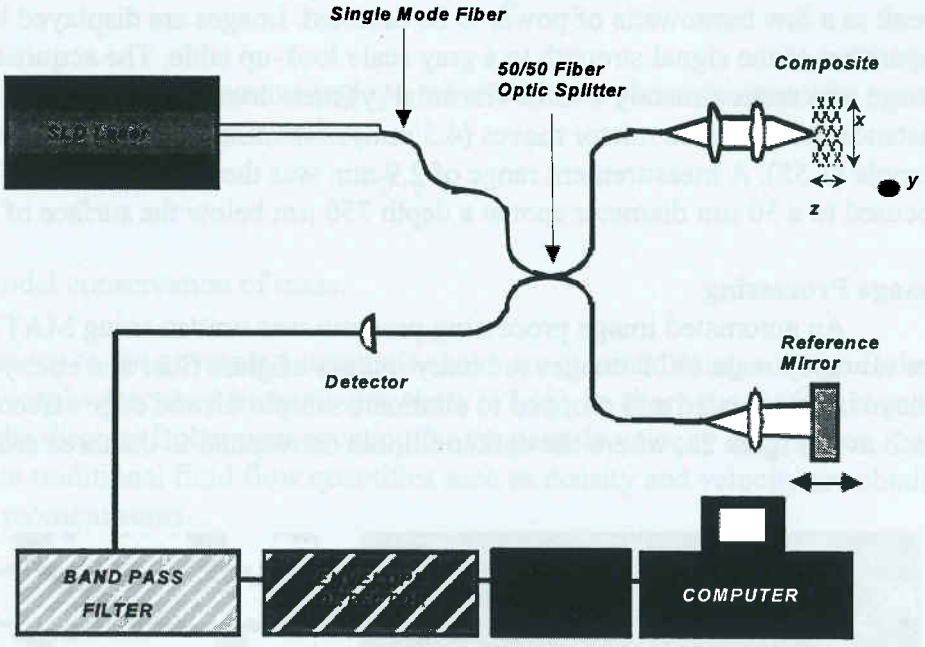

Figure 1. Schematic representation of the solid state laser and OCT system layout.

of up to 15 mW and a spectral bandwidth of 40 nm, corresponding to an axial spatial

resolution of ≈ 20 μm. The laser light was coupled into a single-mode fiber-optic Michelson interferometer and delivered to both the reference mirror and the sample. The reference mirror was mounted on a rotating galvanometer, which is driven with a sawtooth voltage waveform. Transverse scanning was performed using a computer controlled motorized stage to translate the sample.

The fiber optic interferometer consists of single-mode optical fiber coupled with a 50/50 fiber optic splitter that illuminates both the sample and a linearly translating reference mirror. Light reflected from the reference mirror recombines with light back-scattered and reflected from the sample at the 50/50 splitter to create a temporal interference pattern which is measured with a photodiode detector. The resulting interference patterns are present only when the optical path difference of the reference arm matches that of the sample arm to within the coherence length of the source. The axial, or y, spatial resolution that can be obtained with OCT is determined by the coherence length, or inverse spectral width, of the source and is typically 10 to 20 μm. The source is typically a superluminescent diode laser. The transverse, or x, spatial resolution of OCT is determined by the focal spot size on the sample which is typically 20 to 40 μm. The ultimate limitation on the depth of penetration within the sample is the attenuation of light caused by scattering. Three-dimensional images of the sample are obtained by rastering the sample in x between successive OCT measurements along the z-axis.

The interferometric signal was electronically filtered with a bandpass centered on the fringe or heterodyne frequency. The filtered fringe waveform is then demodulated, digitized and stored on a computer. The high dynamic range of this system allows back-reflections as weak as a few femtowatts of power to be detected. Images are displayed by mapping the logarithm of the signal strength to a gray scale look-up table. The acquisition time for each image was approximately 1 min. The axial (y) measurement range is determined by the distance the reference mirror moves (4.5 mm) normalized by the refractive index of the sample (1.55). A measurement range of 2.9 mm was therefore available. The probe beam was focused to a 30 μm diameter spot at a depth 750 μm below the surface of the sample.

Image Processing

An automated image processing program was written using MATLAB 5.1 to convert the raw gray scale OCT images to binary images of glass fiber and epoxy (Figure 2). The raw image is first rotated and cropped to eliminate sample tilt and edge effects, yielding an image such as in Figure 2a, where the darker ellipses correspond to the three cross-sectional layers

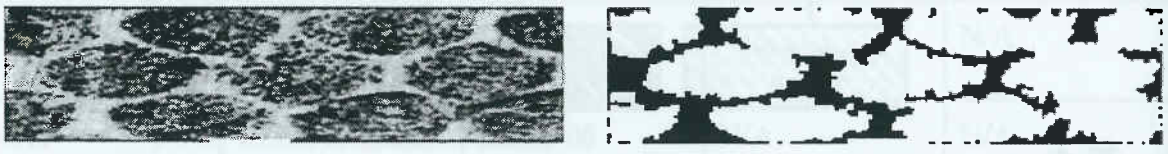

A. *B.*

Figure 2. Original grayscale OCT image of the epoxy/ unidirectional E-glass composite. (A.), Binary OCT image after automated image processing (B.).

of fiber tows while the lighter regions are due to the epoxy. The image is then doubled in size by linear interpolation of adjacent pixels to minimize any artificial alteration of the tow size in subsequent image processing. To increase the contrast between the darker tows and the lighter epoxy regions, a variance image is created replacing the intensity value of a 2x2 cluster of pixels with the standard deviation of that cluster. In the next two steps, spurious light pixels within the tow regions and vertical lines corresponding to detector saturation are eliminated. Using the automated program, the boundaries of the tows are determined and a binary image (Figure 2b) is formed. An additional operation may be performed to smooth the rough boundaries of the tows. The resulting binary image is then used as input for the permeability calculations.

PERMEABILITY PREDICTION USING LATTICE BOLTZMANN METHOD

Lattice Boltzmann formulation

Modeling the microscale flow in fibrous porous media is complicated by the existence of an open region around the tows, and a porous media inside the tows. Following previous studies [15-19], the Stokes equation, given by

$$\nabla P = \mu \nabla^2 v \tag{2}$$

is used to model flow in the open regions, and the Brinkman equation, given by

$$\nabla P = \mu \nabla^2 v - \frac{\mu}{K} \cdot v \tag{3}$$

is used to model flow in the porous regions, where K is the permeability of the porous tows. In both regions, the continuity equation,

$$\nabla \cdot v = 0 \tag{4}$$

is used to model conservation of mass.

Solutions to the governing equations above are obtained using a lattice Boltzmann method previously described in detail elsewhere [17,18]. In short, the method involves the solution of the discrete Boltzmann equation for the particle velocity distribution function $n_\alpha(x,t)$, where traditional fluid flow quantities such as density and velocity are obtained through the moment sums

$$\rho = m \sum_{\alpha=1}^{N} n_\alpha(x,t) \tag{5}$$

$$u = \frac{m}{\rho(x,t)} \sum_{\alpha=1}^{N} v_\alpha n_\alpha(x,t) \tag{6}$$

where $\rho(x,t)$ and $u(x,t)$ are the macroscopic fluid density and velocity, m is the mass of fluid, v_α are components of the discrete velocity space, and N is the number of velocities comprising the velocity space.

The particle distribution function $n_\alpha(x,t)$ is governed by the discrete Boltzmann equation given by

$$n_\alpha(x+v_\alpha,t+1) = n_\alpha(x,t)+\delta_\alpha(x,t) \tag{7}$$

where $\delta_\alpha(x,t)$ is the collision operator which couples the set of velocity states v_α. Most LB formulations employ the linear "BGK" form [17,18,25] of the collision operator in which the distribution function is expanded about its equilibrium value

$$\delta_\alpha(x,t) = -\frac{n_\alpha(x,t)-n_\alpha^{eq}(x,t)}{\tau} \tag{8}$$

where $n_\alpha^{eq}(x,t)$ is called the equilibrium distribution function and τ is a relaxation time for collisions controlling the rate of approach to equilibrium. The form of the equilibrium distribution function depends on the particular lattice model chosen. The three-dimensional, "d3q15" model [13] which resides on a cubic lattice is used here (d3 indicates the model is three-dimensional, q15 refers to the number of components in the velocity space). For this model, the equilibrium distribution function is given by

$$n_\alpha^{eq} = \frac{1}{9}\rho\left(1+3\frac{(e_\alpha\cdot u)}{c}+\frac{9}{2}\frac{(e_\alpha\cdot u)^2}{c^2}-\frac{3}{2}\frac{u^2}{c^2}\right), \quad \alpha = 1,6 \tag{9}$$

$$n_\alpha^{eq} = \frac{1}{72}\rho\left(1+3\frac{(e_\alpha\cdot u)}{c}+\frac{9}{2}\frac{(e_\alpha\cdot u)^2}{c^2}-\frac{3}{2}\frac{u^2}{c^2}\right), \quad \alpha = 7,14 \tag{10}$$

$$n_{15}^{eq} = \frac{2}{9}\rho\left(1-\frac{3}{2}\frac{u^2}{c^2}\right) \tag{11}$$

where $v_\alpha = ce_\alpha$, c is the lattice velocity, and e_α are the unit vectors in each of the 15 different directions on the discretized lattice.

Flow Calculation and Permeability Computation with Darcy's Law

Permeability for different flow directions was computed by imposing a constant pressure along opposite faces of the lattice in the desired direction and integrating the system of equations above to steady-state. Estimates for the intra-tow permeability values were obtained from the formulas given in [15]. The steady-state velocity field at the inlet was integrated over the surface to obtain the flow rate, Q, and this was used in the formula

$$K_{eff} = \frac{\mu Q L}{A \Delta P} \tag{12}$$

to obtain the effective permeability, K_{eff}, for the desired flow direction.

CALCULATED RESULTS COMPARED TO EXPERIMENTAL RESULTS

The results from the permeability calculations are shown in Table 2. Table 2 also includes a summary of the experimental permeability. The experimental axial permeability is the average of the four saturated flow measurements given in Table 1, along with the standard deviation of those four measurements. The experimental transverse permeability is the average axial permeability multiplied by the anisotropy value obtained from the radial

Table 2. Calculated results compared to experimental results

Sample	Image Processing	Image set	Axial K, K_a, cm^2, $x10^6$	Transverse K, K_t, cm^2, $x10^6$	Anisotropy, K_a/K_t
Experimental	N/A	N/A	5.3 ± 2.6	0.75	7.0
Calculation 1	Manual	87-91	4.45	0.882	5.06
Calculation 2	Manual	75-95	3.81	0.992	4.11
Calculation 3	Automated, No smoothing	75-95	2.83	0.654	4.32
Calculation 4	Automated, Smoothing	75-95	3.18	0.991	3.21
Calculation 5	Automated, Smoothing	4-24	5.09	0.934	5.45
Calculation 6	Manual, Roughened	75-95	2.73	0.662	4.12
Calculation 7	Manual, Dilated	75-95	2.99	0.767	3.90

flow experiment. Although the computed axial permeability values are lower than the experimental axial permeability, the agreement is quite reasonable considering the large experimental uncertainty. Moreover, the calculated transverse permeability values are larger than the experimental value due to the experimental anisotropy value that is larger than the calculated values. Clearly, the combination of OCT and lattice Boltzmann calculations have bracketed the experimental results for this particular example.

The raw OCT images were processed in two different ways to provide the calculated permeability values in Table 2. For the "Manual" method, the tow outlines were drawn by sight and filled in. Calculations using the "Automated" method used OCT images that were processed as described above in the Image Processing section.

There are two important points illustrated by the results in Table 2. First, large local variations in permeability are predicted, as shown by comparing Calculations 1 and 2, or by comparing Calculations 4 and 5. Calculation 1 was performed on a small set of 5 images (images 87-91) that make up a subset of the images used for Calculation 2 (images 75-95), illustrating that within a small region of material the permeability can vary substantially. Calculations 4 and 5 were performed on separate sets of images within the same composite sample, illustrating substantial permeability variation from region to region. Second, comparing Calculations 2, 3, and 4 illustrates the importance of image processing. The calculated permeability value is strongly affected by the method used to process the images.

The different image processing methods produced slightly different binary images, and those differences were characterized by small differences in the fraction of the image area occupied by tows as well as by differences in the roughness of the tow boundaries. Calculations 6 and 7 indicate that the tow roughness is the dominant factor controlling the differences observed in the permeability values calculated using the different image processing methods. Note that roughening the tow surfaces caused a larger decrease in the permeability (compare Calculation 6 to 2) than did simply dilating the tow sizes (compare Calculation 7 to 2).

SUMMARY

The microstructure of a glass reinforced composite was accurately and rapidly obtained using optical coherence tomography. OCT images were processed and input into a microscale flow model for permeability prediction. The axial and transverse permeabilities were predicted and compared to a set of experimental measurements. The agreement was quite good considering the experiments had an uncertainty of roughly 50%. Further examination of the results highlighted the importance of boundary roughness generated during image processing.

ACKNOWLEDGEMENTS

This work was supported in part by a grant from the US Department of Commerce, contract

70NANB6H0092. We gratefully acknowledge technical contributions of Drs. Juergen Herrmann, Wolfgang Drexler, and Mr. Rohit Prasankumar.

REFERENCES

1. P. Beardmore and D. Hunston, *Polymer Composite Processing, An Industry Workshop*, US Dept. Of Commerce, NBSIR 87-3686 (1987).

2. C.D. Rudd, A.C. Long, P. McGeehin and P. Smith, *Polymer Composites*, **17(1)**, 52 (1996).

3. J.K Spoerre, *Integrated Product and Process Design for Resin Transfer Molded Parts*, PhD Thesis, Florida State University (1995).

4. R.S. Parnas, A.J. Salem, K.N. Kendall and M.V. Bruschke, Eds., *Report on the Workshop on Manufacturing Polymer Composites by Liquid Molding*, US Dept. Of Commerce, NISTIR 5373 (1993).

5. T.L. Luce, S.G. Advani, J.G. Howard and R.S. Parnas, *Polymer Composites*, **16(6)**, 446 (1995).

6. R.S. Parnas, C.R. Schultheisz and S. Ranganathan, *Polymer Composites*, **17(1)**, 4 (1996).

7. H. D'Arcy, *Les Fontaines Publiques de la Ville de Dijon*, Dalmont, Paris (1856).

8. P.M. Adler, *Porous Media*, Butterworth-Heinemann, Boston (1992).

9. K.L. Adams, W.B. Russel and L. Rebenfeld, *Int.J.Multiphase Flow*, **14(2)**, 203 (1988).

10. R.S. Parnas, Ch 8, in *Resin Transfer Moulding for Aerospace Applications*, T.K. Kruckenberg, ed. Chapman Hall, London, in press (1999).

11. R.S. Parnas and A.J. Salem, *Polymer Composites*, **14(5)**, 383 (1993).

12. D.L. Woerdeman, F.R. Phelan and R.S. Parnas, *Polymer Composites*, **16(6)**, 470 (1995).

13. B. Miller and H.L. Friedman, *The New Nonwovens World*, **2(3)**, 83 (1993).

14. R. Parnas, K. Flynn and M. Dal-Favero, *Polymer Composites*, **18(5)**, 623 (1997).

15. S. Ranganathan, G. Wise, F. Phelan, R. Parnas and S. Advani, *Advanced Composites X: Proceedings of the 10th Annual ASM/ESD Advanced Composites Conference and Exposition (ACCE94)*, ASM International, 309 (1994).

16. F. Phelan and G. Wise, *Composites: Part A*, **27A(1)**, 25 (1996).

17. M. Spaid and F. Phelan, *Phys. Fluids*, **9(9)**, 2468 (1997).

18. M. Spaid and F. Phelan, *Composites: Part A*, **29A**, 749 (1998).

19. S. Ranganathan, R. Easterling, S. Advani and F. Phelan, *Polymers & Polymer Composites*, **6(2)**, 63, (1998).

20. D. Huang, E. Swanson, C. Lin, J. Schuman, W. Stinson, W. Chang, M. Hee, T. Flotte, K. Gregory, C. Puliafito and J. Fujimoto, *Science*, **254**, 1178, (1991).

21. J. Fujimoto, M. Brezinski, G. Tearney, S. Boppart, B. Bouma, M. Hee, J. Southern and E. Swanson, *Nature Medicine*, **1**, 970, (1995).

22. M. Bashkansky, M. Duncan, M. Kahn, D. Lewis and J. Reintjes, *Opt. Lett.*, **22**, 61 (1997).

23. Identification of a commercial product is made only to facilitate experimental reproducibility and to adequately describe experimental procedure. In no case does it imply endorsement by NIST or imply that it is necessarily the best product for the experimental procedure.

24. J. Dunkers, R. Parnas, C. Zimba, R. Peterson, K. Flynn, J. Fujimoto and B. Bouma, *Composites, Part A*, **30A**, 139 (1999).

25. S. Hou, *Lattice Boltmann Method for Incompressible, Viscous Flow*, Ph.D. Dissertation, Department of Mechanical Engineering, Kansas State University, Manhattan, Kansas, (1995).